arXiv:1704.00599v1 [gr-qc] 30 Mar 2017

GiRaFFE: An Open-Source General Relativistic Force-Free Electrodynamics Code

Zachariah B. Etienne[1,2], Mew-Bing Wan[3], Maria C. Babiuc[4], Sean T. McWilliams[2,5], Ashok Choudhary[5]

[1] Department of Mathematics, West Virginia University, Morgantown, WV 26506, USA

[2] Center for Gravitational Waves and Cosmology, West Virginia University, Chestnut Ridge Research Building, Morgantown, WV 26505, USA

[3] Institute for Advanced Physics and Mathematics, Zhejiang University of Technology, Hangzhou, 310032, China

[4] Department of Physics, Marshall University, Huntington, WV 25755, USA

[5] Department of Physics & Astronomy, West Virginia University, Morgantown, WV 26506, USA

Abstract. We present `GiRaFFE`, the first open-source general relativistic force-free electrodynamics (GRFFE) code for dynamical, numerical-relativity generated spacetimes. `GiRaFFE` adopts the strategy pioneered by McKinney [30] and modified by Paschalidis and Shapiro [43] to convert a GR magnetohydrodynamic (GRMHD) code into a GRFFE code. In short, `GiRaFFE` exists as a modification of `IllinoisGRMHD` [19], a user-friendly, open-source, dynamical-spacetime GRMHD code. Both `GiRaFFE` and `IllinoisGRMHD` leverage the Einstein Toolkit's highly-scalable infrastructure [13, 47] to make possible large-scale simulations of magnetized plasmas in strong, dynamical spacetimes on adaptive-mesh refinement (AMR) grids. We demonstrate that `GiRaFFE` passes a large suite of both flat and curved-spacetime code tests passed by a number of other state-of-the-art GRFFE codes, and is thus ready for production-scale simulations of GRFFE phenomena of key interest to relativistic astrophysics.

PACS numbers: 52.30.-q, 52.27.Ny, 04.25.D-, 04.25.dg, 04.30.-w, 95.85.Sz, 04.70.Bw

1. Introduction

With LIGO's first detections of gravitational waves [1, 2], the era of gravitational wave (GW) astronomy has arrived, and an exciting new window on the Universe has been opened. The prospect of multimessenger observations stemming from an observed gravitational wave source with coincident electromagnetic (EM) and/or neutrino signals promises to provide far deeper insights into the extremely violent processes that generate these GW signals.

0.4 seconds after the first GW detection, a weak gamma-ray burst (GRB) lasting 1 second was observed in the hard X-ray band (> 50keV) by the Fermi Gamma-ray Burst Monitor, in a region of the sky overlapping the very large LIGO localization area [14]. Stellar-mass black hole binaries (BHBs) are not generally expected to exist in matter-rich environments assumed necessary to power such a GRB, suggesting that the coincidence is most likely due to a statistical/systematic fluke in the Fermi data, but would indicate the unexpected presence of a tenuous plasma surrounding the BHB if the coincidence proved genuine [6]. Regardless, if Nature does provide an electromagnetic (EM) counterpart to the GW emission from BHBs—whether from a stellar-mass binary observable by Advanced LIGO, intermediate-mass or massive BHBs observable by the Laser Interferometer Space Antenna (LISA), or supermassive BHBs observable by pulsar timing arrays—it will most likely be driven by the interaction of the BHB with a tenuous plasma.

BHBs are not the only systems in which strong-field gravitation could affect the dynamics of a tenuous, magnetically-dominated plasma. Neutron star (NS) and pulsar magnetospheres are other prime examples in which magnetic field lines originating from the intense gravitational fields at the stellar surface continue into the magnetosphere just outside the NS. So just as in the case of BHBs, fully self-consistent modeling of these systems requires that the plasma dynamics be followed in the context of nonperturbative solutions to the general relativistic field equations.

Future gravitational wave detections by LIGO may originate from binary NSs or black hole–neutron star (BHNS) binary mergers. Observing an electromagnetic counterpart to these incredibly violent processes may provide deep insights not only into the behavior of matter at extreme densities, but also the mechanism behind short GRBs. The behavior of binary NS magnetospheres during their late-inspiral phase may launch EM counterparts prior to and during a GW detection. In the case of BHNS binaries, the motion of the BH through the magnetic field of its NS companion during the inspiral can form a unipolar inductor, beaming radiation over the full sky each orbit [18, 22, 33, 41]. At the end of the inspiral, either for a BHNS with a sufficiently light, highly-spinning BH or a BNS with sufficiently high mass, NS disruption and subsequent accretion onto the BH (formed from hypermassive NS collapse in the case of BNS) can launch a classic short GRB jet [7, 34, 42, 40, 46].

In all of the aforementioned systems, the dynamics driving the EM signal involve a strongly magnetized tenuous plasma accelerating within a curved, often

highly-dynamical spacetime. Properly modeling such dynamics will require that the appropriate general relativistic versions of the equations governing plasma dynamics be chosen. For regions in which the magnetic-to-gas-pressure ratios are less than or are of order unity, such as the interior of a NS or an accretion disk surrounding a BH or BHB, the plasma dynamics are well-described by the equations of ideal general relativistic magnetohydrodynamics (GRMHD). But as these ratios far exceed unity—as is the case for tenuous plasma outside BHs, BHBs, and NSs—the GRMHD equations become stiff, and solving instead the equations of general relativistic force-free electrodynamics (GRFFE) is far more numerically tractable. The equations of GRFFE are a limiting case of ideal GRMHD, in which the magnetic fields (as opposed to hydrodynamic densities and pressures) entirely drive the plasma dynamics.

While technically it would be best to employ an algorithm that can accommodate arbitrary magnetic-to-gas-pressure ratios, in practical terms, the dynamics of many systems of interest are well approximated by either the GRMHD or GRFFE limits. In exceptional cases such as the boundary between a NS and its magnetosphere, an optimal method would allow for feedback from the ideal GRMHD region into the GRFFE region, and vice-versa. To this end, methods have been developed for feeding information from the ideal GRMHD region of the NS interior into the magnetosphere, which is well-described by the equations of GRFFE [36, 43]. These methods effectively impose a dynamical boundary condition for the surface of the magnetosphere (i.e., the surface outside of which the equations of GRFFE are solved). While GRMHD flows can inform regions well-described by the GRFFE equations, the reverse is not yet possible with current GRFFE prescriptions, as the GRFFE equations destroy information about hydrodynamic pressures and densities—two essential quantities that must be specified within the ideal GRMHD framework.

The GRFFE equations and their application in modeling important astrophysical scenarios have a long history in the literature and continue to be an active area of study by many independent groups. Komissarov [25] was one of the first to develop a conservative GRFFE formalism and numerical code in the context of strong-field spacetimes to study the properties of the plasma-filled magnetospheres of black holes [26, 27, 28]. Later, McKinney would introduce a general relativistic force-free (GRFFE) numerical formulation that, through minimal modification of a general relativistic magnetohydrodynamic (GRMHD) code, enables evolutions of the GRFFE equations of motion [30, 31, 32]. Adopting such a prescription, Palenzuela *et al* [38, 37] studied the interaction of binary and single black holes with ambient magnetic fields within the GRFFE approximation, observing the formation of a dual jet morphology when BHBs orbited within a uniform background magnetic field, and a single jet in the context of a single, spinning black hole—a dramatic confirmation of the Blandford-Znajek mechanism [8]. Motivated in part by these results, as well as a desire to more deeply explore important GRFFE phenomena in this age of multimessenger astrophysics, multiple other independent groups have developed GRFFE codes [3, 10, 11, 35, 39, 44, 45, 52, 48].

One GRFFE code of particular interest to work presented here is that of Paschalidis and Shapiro [43], who extended McKinney's prescription for GRMHD-to-GRFFE code conversion. In part this extension focused on smoothly matching general relativistic ideal MHD to its force-free limit, so that GRMHD dynamics can inform regions of the physical domain more accurately modeled by a GRFFE code. `IllinoisGRMHD` is an open-source rewrite of the GRMHD code on which Paschalidis and Shapiro's GRFFE code is based, and the code we present here, `GiRaFFE`‡, is based on `IllinoisGRMHD`. Unlike the code of Paschalidis and Shapiro, `GiRaFFE` is a pure GRFFE code, not currently designed to match the equations of GRMHD to its force-free limit.

`GiRaFFE` represents the first open-source GRFFE code designed for dynamical spacetime simulations. Based on `IllinoisGRMHD`, `GiRaFFE` employs the prescription devised by McKinney [30] and refined by Paschalidis and Shapiro [43] for converting a GRMHD code into a GRFFE code. Like the code on which it was based, `GiRaFFE` is fully compatible with the Einstein Toolkit adaptive-mesh refinement (AMR) Cactus/Carpet infrastructure [13, 47], and is therefore highly scalable, to tens of thousands of cores. Also, `GiRaFFE` is quite compact, existing in only about 1,600 lines of code. For dynamical-spacetime GRFFE simulations, `GiRaFFE` may be immediately coupled to McLachlan [9], a state-of-the-art, open-source, `Kranc`-generated [24, 29] spacetime evolution module within the Einstein Toolkit.

The rest of the paper is structured as follows. In Sec. 2, we review our adopted GRFFE formalism and in Sec. 3 how these equations are solved within the `GiRaFFE` code. Then in Sec. 4, we present a large suite of GRFFE code tests, and finally in Sec. 5 we summarize the paper and present plans for future work.

2. Adopted GRFFE Formalism

All equations are written in geometrized units, such that $G = c = 1$, and Einstein notation is chosen for implied summation. Greek indices span all 4 spacetime dimensions, and Latin indices span only the 3 spatial dimensions.

The line element for our spacetime in standard 3+1 form is given by

$$ds^2 = -\alpha^2 dt^2 + \gamma_{ij}(dx^i + \beta^i dt)(dx^j + \beta^j dt), \tag{1}$$

where αdt denotes the proper time interval between adjacent spatial hypersurfaces separated by coordinate times $t = t_0$ and $t = t_0 + dt$, β^i the magnitude of the spatial coordinate shift between adjacent hypersurfaces, and γ_{ij} is the three-metric within a given hypersurface at coordinate time t.

Our 3+1 GRFFE formalism is written in terms of electric and magnetic fields as measured by an observer co-moving and normal to the spatial hypersurface, with 4-velocity $n^\mu = (1/\alpha, -\beta^i/\alpha)$. In terms of the Faraday tensor $F^{\mu\nu}$, the electric E^ν and

‡ `GiRaFFE` and both initial data modules (`GiRaFFEfood` and `ShiftedKerrSchild`) are open source (under the 2-clause BSD or GNU General Public License, version 2.0 or greater) and can be downloaded from `https://bitbucket.org/zach_etienne/wvuthorns/`.

magnetic B^ν fields in this frame are given by

$$E^\nu = n_\mu F^{\mu\nu} \tag{2}$$

$$B^\nu = -\frac{1}{2} n_\mu \epsilon^{\nu\mu\sigma\eta} F_{\sigma\eta} = n_\mu {}^*F^{\mu\nu}, \tag{3}$$

where ${}^*F^{\mu\nu}$ is the dual of the Faraday tensor.

In ideal MHD, the electric field vanishes for observers moving *parallel* to the plasma with 4-velocity u^ν:

$$F^{\mu\nu} u_\nu = -\sqrt{4\pi} E^\mu_{(u)} = 0. \tag{4}$$

I.e., when an observer moves in a direction parallel to the magnetic field lines, the electric field vanishes. This is simply a statement of Ohm's law for the case of perfect conductivity. One implication of perfect conductivity is that "magnetic field lines remain attached to the fluid elements they connect"—the so-called "frozen-in condition of MHD". In addition, so long as $F^{\mu\nu} \neq 0$, the ideal MHD condition implies that

$$F^{\mu\nu} F_{\mu\nu} = 2(B^2 - E^2) > 0 \quad \rightarrow \quad B^2 > E^2, \quad \text{and} \tag{5}$$

$${}^*F^{\mu\nu} F_{\mu\nu} = 4 E_\mu B^\mu \qquad = 0. \tag{6}$$

See, *e.g.*, [25, 43] for further discussion.

In addition to the ideal MHD condition $E^\mu_{(u)} = 0$, force-free electrodynamics also assumes that the plasma dynamics are completely driven by the electromagnetic fields (as opposed to, e.g., fluid pressure gradients). This implies that the stress-energy of the plasma (where $T^{\mu\nu}$ is the stress-energy tensor) is completely dominated by the electromagnetic terms, which yields the conservation equation [38, 39]:

$$\nabla_\nu T^{\mu\nu} \approx \nabla_\nu T^{\mu\nu}_{\rm EM} = -F^{\mu\nu} J_\nu = 0 \tag{7}$$

$$\rightarrow \rho E^i + n_\nu \epsilon^{\nu ijk} J^{(3)}_j B_k = 0. \tag{8}$$

where $\epsilon^{\nu ijk}$ is the Levi-Civita tensor, $J^{(3)}_i$ is the 3-current, and ρ the charge density. From these, the 4-current can be expressed $J^\nu = \rho n^\nu + \gamma^\nu_\mu J^\mu = \gamma^\nu_\mu J^\mu$ ($\rho = 0$ in the force-free approximation).

The left-hand side of Eq. 8 is simply the relativistic expression for the Lorentz force, indicating that indeed the Lorentz force is zero in force-free electrodynamics. Combining this force-free assumption with the ideal MHD condition (see, e.g., [25, 43] for full derivation), two additional constraints emerge:

$$B_i E^i = 0, \quad \text{and} \tag{9}$$

$$B^2 > E^2. \tag{10}$$

Under these additional constraints, the GRFFE evolution equations consist of the Cauchy momentum equation and the induction equation (see [25, 30, 43] for derivation):

(i) We choose to write the Cauchy momentum equation in conservative form and in terms of the densitized spatial Poynting flux one-form $\tilde{S}_i = \sqrt{\gamma} S_i$,

$$\partial_t \tilde{S}_i + \partial_j \left(\alpha \sqrt{\gamma} T^i_{{\rm EM}\, i} \right) = \frac{1}{2} \alpha \sqrt{\gamma} T^{\mu\nu}_{\rm EM} \partial_i g_{\mu\nu}, \tag{11}$$

where S_i can be derived from the expression of the Poynting one-form,

$$S_\mu = -n_\nu T^\nu_{\mathrm{EM}\mu}. \tag{12}$$

(ii) The induction equation in the force-free limit becomes, in terms of the densitized magnetic field $\tilde{B}^i = \sqrt{\gamma} B^i$,

$$\partial_t \tilde{B}^i + \partial_j \left(v^j \tilde{B}^i - v^i \tilde{B}^j \right) = 0, \tag{13}$$

where $v^j = u^j/u^0$ is the *minimum* plasma 3-velocity that satisfies $F^{\mu\nu} u_\nu = 0$. This choice of v^j is often referred to as the *drift* velocity, which can be defined in terms of known variables as

$$v^i = 4\pi\alpha \frac{\gamma^{ij} \tilde{S}_j}{\sqrt{\gamma} B^2} - \beta^i. \tag{14}$$

3. Numerical Algorithms

We briefly review the numerical algorithms employed in `GiRaFFE` to solve the equations of GRFFE as outlined in Sec. 2.

`GiRaFFE` fully supports Cartesian adaptive mesh refinement (AMR) grids via the Cactus/Carpet [47] infrastructure within the Einstein Toolkit [13].

As in `IllinoisGRMHD`, `GiRaFFE` guarantees that the magnetic fields remain divergenceless to roundoff error *even on AMR grids* by evolving the vector potential $\mathcal{A}_\mu = \Phi n_\mu + A_\mu$, where A_μ is spatial ($A_\mu n^\mu = 0$), instead of the magnetic fields directly. The vector potential fields exist on a staggered grid (as defined in Table 1 of Ref. [19]) such that our magnetic fields are evolved according to the flux constrained transport (FluxCT) algorithm of Refs. [5, 50].

Our choice of vector potential requires that we solve the vector potential version of the induction equation

$$\partial_t A_i = \epsilon_{ijk} v^j B^k - \partial_i (\alpha\Phi - \beta^j A_j), \tag{15}$$

where $\epsilon_{ijk} = [ijk]\sqrt{\gamma}$ is the anti-symmetric Levi-Civita tensor and γ is the 3-metric determinant, which in a flat spacetime in Cartesian coordinates reduces to 1. B^k in Eq. 15 is computed from the vector potential via

$$B^i = \epsilon^{ijk} \partial_j A_k = \frac{[ijk]}{\sqrt{\gamma}} \partial_j A_k. \tag{16}$$

Φ is evolved via an additional electromagnetic gauge evolution equation, which was devised specifically to avoid the buildup of numerical errors due to zero-speed characteristic modes [20] on AMR grids. Our electromagnetic gauge is identical to the Lorenz gauge, but with an exponential damping term with damping constant ξ [21]:

$$\partial_t \left[\sqrt{\gamma}\Phi\right] + \partial_j \left(\alpha\sqrt{\gamma} A^j - \beta^j \left[\sqrt{\gamma}\Phi\right] \right) = -\xi\alpha \left[\sqrt{\gamma}\Phi\right]. \tag{17}$$

Step 0: Initial data: In addition to 3+1 metric quantities in the Arnowitt-Deser-Misner (ADM) formalism [4], `GiRaFFE` requires that the "Valencia" 3-velocity $\bar{v}^i$ and

vector potential one-form A_μ be set initially. Regarding the former, the "Valencia" 3-velocity $\bar{v}^i$ is related to the 3-velocity appearing in the induction equation v^i via

$$v^i = \frac{u^i}{u^0} = \alpha \bar{v}^i - \beta^i. \tag{18}$$

As for A_μ, for all cases in this paper, we set the evolution variable $\left[\sqrt{\gamma}\Phi\right] = 0$ initially, and A_i is set based on our initial physical scenario.

After v^i and A_μ are set, B^i is computed via Eq. 16, and then the evolution variable $\tilde{S}_i$ is given by

$$\tilde{S}_i = \frac{\gamma_{ij}(v^j + \beta^j)\sqrt{\gamma}B^2}{4\pi\alpha}. \tag{19}$$

Step 1: Evaluation of evolution equations: In tandem with the high-resolution shock-capturing (HRSC) scheme within `GiRaFFE`, the Runge-Kutta fourth-order (RK4) scheme is chosen to march our evolution variables A_i and $\tilde{S}_i$ forward in time from their initial values, adopting precisely the same reconstruction and Riemann solver algorithms as in `IllinoisGRMHD` (see Ref. [19] for more details). In short, A_i and $\tilde{S}_i$ are evolved forward in time using the Piecewise Parabolic Method (PPM) [12] for reconstruction and a Harten-Lax-van Leer (HLL)-based algorithm [23, 17] for approximately solving the Riemann problem. Meanwhile, spatial derivatives within $\left[\sqrt{\gamma}\Phi\right]$'s evolution equation (Eq. 17) are evaluated via finite difference techniques (as in `IllinoisGRMHD`).

Step 2: Boundary conditions on A_μ: At the end of each RK4 substep, the evolved variables A_i and $\tilde{S}_i$ have been updated at all points except the outer boundaries. So next the outer boundary conditions on A_i and $\left[\sqrt{\gamma}\Phi\right]$ are applied. As no exact outer boundary conditions typically exist for systems of interest to `GiRaFFE`, we typically take advantage of AMR and push our outer boundary out of causal contact from the physical system of interest. However, to retain good numerical stability, we apply "reasonable" outer boundary conditions. Specifically, values of A_i and $\left[\sqrt{\gamma}\Phi\right]$ in the interior grid are linearly extrapolated to the outer boundary.

Step 3: Computing B^i: B^i is next computed from A_i via Eq. 16.

Step 4: Applying GRFFE constraints & computing v^i: Truncation, roundoff, and undersampling errors will at times push physical quantities into regions that violate the GRFFE constraints. To nudge the variables back into a physically realistic domain, we apply the same strategy as was devised in Ref. [43] to guarantee that the GRFFE constraints remain satisfied:

First, we adjust $\tilde{S}_i$ via

$$\tilde{S}_i \to \tilde{S}_i - \frac{(\tilde{S}_j \tilde{B}^j)\tilde{B}_i}{\tilde{B}^2} \tag{20}$$

to enforce $B^i S_i = 0$, which as shown by Ref. [43], is equivalent to the GRFFE constraint Eq. 9.

Next, we limit the Lorentz factor of the plasma, typically to be 2,000, by rescaling $\tilde{S}_i$ according to Eq. 92 in Ref. [43]. After $\tilde{S}_i$ is rescaled the 3-velocity v^i is recomputed via Eq. 14.

Finally, errors within our numerical scheme dissipate sharp features, so when current sheets appear, they are quickly and unphysically dissipated. This is unfortunate because current sheets lie at the heart of many GRFFE phenomena. So to remedy the situation, we apply the basic strategy of McKinney [30] (that was alsoadopted by Paschalidis and Shapiro [43]) and set the velocity perpendicular to the current sheet $v^{\perp}$ to zero. For example, if the current sheet exists on the $z = 0$ plane, then $v^{\perp} = v^z$, which we set to zero via $n_i v^i = 0$, where $n_i = \gamma_{ij} n^j$ is a unit normal one-form with $n^j = \delta^{jz}$. Specifically, in the case of a current sheet on the $z = 0$ plane, we set

$$v^z = -\frac{\gamma_{xz} v^x + \gamma_{yz} v^y}{\gamma_{zz}} \tag{21}$$

at all gridpoints that lie within $|z| \leq 4\Delta z$ of the current sheet.

Step 5: Boundary conditions on v^i: v^i is set to zero at a given face of our outermost AMR grid cube unless the velocity is *outgoing*. Otherwise the value for the velocity is simply copied from the interior grid to the nearest neighbor on a face-by-face basis.

After boundary conditions on v^i are updated, all data needed for the next RK4 substep have been generated, so we return to Step 1.

4. Results

We focus on the same suite of flat and curved spacetime background code validation tests as in Paschalidis *et al.* [43], who in turn take cues from code validation tests of Komissarov [25] and McKinney [30]. The tests are designed to push GRFFE codes to their limits, while at the same time providing either an exact or well-described qualitative solution to which a code can be demonstrated to converge with increasing numerical resolution.

The GRFFE code described in Ref. [43] exists as a modification to `OrigGRMHD`, the original GRMHD code of the Illinois Numerical Relativity group. `IllinoisGRMHD` is a complete open-source rewrite of `OrigGRMHD`, demonstrated to generate results that agree to roundoff error with `OrigGRMHD`. `GiRaFFE` is based on a modification of `IllinoisGRMHD`, so we expect that the results of the tests we perform here would match closely with those presented in Ref. [43]. However, we are unable to demonstrate roundoff-level agreement between `GiRaFFE` and the code of Ref. [43] since we do not have access to the latter. So wherever possible, we attempt to duplicate figures presented in Ref. [43] with `GiRaFFE` so as to make direct comparison straightforward. In short, we find excellent qualitative agreement between `GiRaFFE` and the results of Ref. [43].

The rest of this section is organized as follows. Section 4.1 presents our flat-spacetime code validation results, and Sec. 4.2 details curved-spacetime results.

4.1. Flat spacetime background tests

Our flat spacetime tests include a suite of five tests in one spatial dimension (i.e., our "1D code tests"), as well as the aligned rotator test, which is a toy model of a pulsar

Test name (wave speed)	Vector potential	Electric field
Fast wave ($\mu = 1$)	$A_x = 0,$ $A_y = 0,$ $A_z = y + \begin{cases} -x - 0.0075 & \text{if } x \leq -0.1, \\ 0.75x^2 - 0.85x & \text{if } -0.1 < x < 0.1, \\ -0.7x - 0.0075 & \text{if } x \geq 0.1. \end{cases}$	$E^x = 0,$ $E^y = 0,$ $E^z = -B^y.$
Alfvén wave ($\mu = -0.5$)	$A_x = 0,$ $A_y = \begin{cases} \gamma_\mu x - 0.015 & \text{if } \gamma_\mu x \leq -0.1, \\ 1.15\gamma_\mu x - 0.03\cos(5\pi\gamma_\mu x)/\pi & \text{if } -0.1 < \gamma_\mu x < 0.1, \\ 1.3\gamma_\mu x - 0.015 & \text{if } \gamma_\mu x \geq 0.1, \end{cases}$ $A_z = y - \gamma_\mu(1-\mu)x.$	$E^x = -B'^z,$ $E^y = \gamma_\mu\mu B'^z,$ $E^z = \gamma_\mu(1.0-\mu).$
Degenerate Alfvén wave ($\mu = 0.5$)	$A_x = 0,$ $A_y = \begin{cases} -0.8/\pi & \text{if } \gamma_\mu x \leq -0.1, \\ -(0.8/\pi)\cos[2.5\pi(\gamma_\mu x + 0.1)] & \text{if } -0.1 < \gamma_\mu x < 0.1, \\ 2(\gamma_\mu x - 0.1) & \text{if } \gamma_\mu x \geq 0.1, \end{cases}$ $A_z = \begin{cases} -2(\gamma_\mu x + 0.1) & \text{if } \gamma_\mu x \leq -0.1, \\ -(0.8/\pi)\sin[2.5\pi(\gamma_\mu x + 0.1)] & \text{if } -0.1 < \gamma_\mu x < 0.1, \\ -0.8/\pi & \text{if } \gamma_\mu x \geq 0.1. \end{cases}$	$E^x = 0,$ $E^y = \gamma_\mu\mu B'^z,$ $E^z = -\gamma_\mu\mu B'^y.$
Three waves (stationary Alfvén: $\mu = 0$, fast right-going: $\mu = 1$, fast left-going: $\mu = -1$)	$A_x = 0,$ $A_y = 3.5x\mathcal{H}(-x) + 3.0x\mathcal{H}(x),$ $A_z = y - 1.5x\mathcal{H}(-x) - 3.0x\mathcal{H}(x),$ $\mathcal{H}$: Heaviside step function.	$\mathbf{E} = \mathbf{E_a} + \mathbf{E}_+ + \mathbf{E}_-,$ stationary Alfvén wave: $\mathbf{E_a} = \begin{cases} (-1.0, 1.0, 0.0) & \text{if } x \leq 0, \\ (-1.5, 1.0, 0.0) & \text{if } x > 0, \end{cases}$ right-going fast wave: $\mathbf{E}_+ = \begin{cases} (0.0, 0.0, 0.0) & \text{if } x \leq 0, \\ (0.0, 1.0, -1.5) & \text{if } x > 0, \end{cases}$ left-going fast wave: $\mathbf{E}_- = \begin{cases} (0.0, -1.5, 0.5) & \text{if } x \leq 0, \\ (0.0, 0.0, 0.0) & \text{if } x > 0. \end{cases}$
FFE breakdown (none)	$A_x = 0,$ $A_y = \begin{cases} x - 0.2 & \text{if } x < 0, \\ -5.0x^2 + x + 0.2 & \text{if } 0 \leq x \leq 0.2, \\ -x & \text{if } x > 0.2, \end{cases}$ $A_z = y - A_y.$	$\mathbf{E} = (0.0, 0.5, -0.5).$

Table 1: Initial setup for 1D tests. The unprimed and primed fields are in the grid and wave frames respectively, evaluated as functions of the coordinate x. μ is the wave speed relative to the grid frame (in units where $c = 1$), and γ_μ is the corresponding relativistic Lorentz factor. The fields in the wave frame can be obtained from that in the grid frame via a simple Lorentz boost (see Eqs. 104 and 105 in Ref. [43]). From the A_i and E_i given above, all other quantities v^i, B^i and $\tilde{S}_i$ needed for a GRFFE evolution can be computed from Eqs. 12,14, and 16 respectively.

Test name	(N_x, N_y, N_z)	$[x_{min}, x_{max}]$	$[y_{min}, y_{max}]$ & $[z_{min}, z_{max}]$	CFL factor
Fast wave	$(1280, 32, 32)$	$[-4.0, 4.0]$	$[-0.025, 0.025]$	0.5
Alfvén wave				
Degen. Alfvén				
Three waves				
FFE breakdown	$(200, 8, 8)$	$[-0.4, 0.6]$	$[-0.02, 0.02]$	

Table 2: Grid setup for 1D tests.

Test name	Vector potential	Electric field
Split Monopole	$A_r = -\frac{Ca}{8}\lvert\cos\theta\rvert\times \left(1+\frac{4M}{r}\right)\sqrt{1+\frac{2M}{r}}$, $A_\phi = CM^2\left(1-\lvert\cos\theta\rvert + a^2 f(r)\cos\theta\sin^2\theta\right).$	$E_r = -\frac{Ca^3}{8\alpha M^3} f'(r)\cos\theta\sin^2\theta$, $E_\theta = -\frac{Ca}{8\alpha}[\sin\theta + a^2 f(r)\sin\theta(2\cos^2\theta - \sin^2\theta)] - \beta^r\sqrt{\gamma}\frac{Ca}{8r^2}\left(1+\frac{4M}{r}\right)$, $E_\phi = \frac{\beta^r}{\alpha M} Ca^2 f'(r)\cos\theta\sin^2\theta$, $f(r) = \frac{r^2(2r-3M)}{8M^3}L\left(\frac{2M}{r}\right) + \frac{M^2+3Mr-6r^2}{12M^2}\ln\frac{r}{2M} + \frac{11}{72} + \frac{M}{3r} + \frac{r}{2M} - \frac{r^2}{2M^2}$, $L(x) = \mathrm{Li}_2(x) + \frac{1}{2}\ln x\ln(1-x)$ for $0 < x < 1$.
Exact Wald	$A_\phi = \frac{C_0}{2} r^2 \sin^2\theta.$	$E_r = 0$, $E_\theta = 0$, $E_\phi = 2MC_0\left(1+\frac{2M}{r}\right)^{-1/2}\sin^2\theta.$
Magnetospheric Wald	$A_i = \frac{C_0}{2}(g_{i\phi} + 2a g_{ti}).$	$\mathbf{E} = 0.$

Table 3: Initial setup for 3D BH spacetime tests. a is the dimensionless spin parameter for the BH with M representing the BH mass. C and C_0 are constants (both set to 1 in our simulations), and $L(x)$ is the dilogarithm function. To avoid the logarithmic divergence as $r \to \infty$, we neglect $f(r)$ and $f'(r)$ terms in our tests, setting them to zero. From the A_i and E_i given above, all other quantities v^i, B^i and $\tilde{S}_i$ needed for a GRFFE evolution can be computed from Eqs. 12, 14, and 16 respectively.

Test name	AMR cube half-side length; Resolution	CFL factor
Split Monopole	$3.125 \times 2^{6-n} M$; $\frac{M}{16} \times 2^{6-n}, \quad n = 1, 2, ..., 6$	$\frac{1}{32}$ for $n = 1$, $\frac{1}{16}$ for $n = 2$, $\frac{1}{8}$ for $n = 3, 4, 5, 6$
Exact Wald	$3.125 \times 2^{6-n} M$; $\Delta x_{\min} \times 2^{6-n}, \quad n = 1, 2, ..., 6$, $\Delta x_{\min} = \frac{M}{12.8}$(L), $\frac{M}{25.6}$(M), $\frac{M}{51.2}$(H)	
Magnetospheric Wald	$3.125 \times 2^{6-n} M$; $\frac{M}{8} \times 2^{6-n}, \quad n = 1, 2, ..., 6$	
Aligned Rotator	$2.94 R_{\rm NS} \times 2^{10-n}$; $\Delta x_{\min} \times 2^{10-n}, \quad n = 1, 2, ..., 10$, $\Delta x_{\min} = 0.0147 R_{\rm NS}$	$\frac{1}{20} \times 2^{n-1}, n = 1, 2, 3$, $\frac{2}{5}$ for $n = 4, ..., 10$

Table 4: Grid setup for 3D tests. $n = 1$ and $\Delta x_{\min}$ represent the coarsest refinement level, and the grid spacing of the finest level respectively. L, M, H denote low, medium, and high resolution respectively. The BH mass M is set to 1 in all tests for numerical convenience (all results are scale-free and can be trivially rescaled to any desired mass), and $R_{\rm NS} = 1$ for the Aligned Rotator test, also for numerical convenience due to the case being scale-free according to $R_{\rm NS}$.

magnetosphere. We largely follow the testing procedures outlined in Refs. [25, 30, 43].

Initial data parameters for the 1D tests are summarized in Table 1, and in Table 3 and Sec. 4.1.6 for the aligned rotator. So that a direct comparison of the test results can be made between our results and those presented in Ref. [43], our grid setups and parameters are chosen to match those in Ref. [43].

1D code test results are summarized in Fig. 1. The solutions for the tests at time t are denoted as $Q(t, x) = Q(0, x + \mu t)$, where Q represents physical quantities B^i, E^i, or v^i, and μ is the wave velocity (in geometrized units with $c = 1$).

4.1.1. Fast Wave The fast wave, either right or left-going, is one of the characteristic waves of an FFE system. This test for a right-going fast wave is based on that originally done in Ref. [25] for an FFE system. Since the fast wave propagates at the speed of light, $\mu = 1$. The analytic solution at time $t = 0.5$ is obtained by shifting the wave at the initial time to the right by $x \to x + 0.5$. Comparing the z-component of the electric field with the numerical solution (top panel of Fig. 1), we see a complete overlap, indicating that our numerical result matches the analytic solution at this high resolution.

4.1.2. Alfvén Wave The right and left-going Alfvén waves are also characteristic waves of an FFE system, and similar to the fast wave, we base this test on the left-going Alfvén

wave test originally performed in Ref. [25]. For the analytic solution, we shift the wave at the initial time by $x \to x - 1$, and compare this with the numerical solution at time $t = 2$. The extremely close overlap between the analytic and numerical solutions, as evidenced in the z-component of the magnetic field, shown in the second-from-top panel of Fig. 1, indicates that `GiRaFFE` reproduces the analytic solution quite well.

4.1.3. Degenerate Alfvén Wave This test is originally performed in Ref. [25] to evolve a system in which the right and left-going Alfvén waves possess the same wave speed. The degenerate Alfvén wave speed is given as [25, 43]:

$$\mu = \frac{B_z E_y - B_y E_z}{B^2}, \tag{22}$$

consistent with the velocity computed via Eq. 14. To compare the analytic and numerical solutions at time $t = 1$, we shift the wave at the initial time by $x \to x + 0.5$. For the y-component of the electric field, we see a very good agreement (middle panel of Fig. 1) between numerical and analytical results.

4.1.4. Three Waves The three waves test initial data are constructed by superposing the stationary Alfvén wave with the right and left-going fast waves. This test was originally performed in Ref. [25]. For the comparison between the analytic and numerical solutions at time $t = 0.5625$, we shift the initial left-going fast wave by $x = -0.5625$ and the initial right-going fast wave by $x = +0.5625$, while maintaining the position of the initial stationary Alfvén wave. The second-from-bottom panel of Fig. 1 demonstrates an almost complete overlap between the analytic and numerical solutions, as expected for this high resolution.

4.1.5. FFE breakdown The FFE breakdown test is originally performed in Ref. [25] to show that systems with left and right states satisfying the FFE conditions may violate these conditions numerically as time progresses. The initial data consists of a transition layer which obeys the FFE conditions, but evolves to a state where it does not [25]. Fig. 1 shows that $B^2 - E^2$ decreases in time and at $t \approx 0.02$, $B^2 - E^2$ approaches zero, signaling the breakdown of the FFE condition [25]. Our results match quite closely to those of Ref. [43].

4.1.6. Aligned Rotator This test is based on that performed in Refs. [28, 31, 48, 43] to study a time-dependent toy model of a pulsar magnetosphere. The test consists of a spherical surface (the "surface of the star") that rotates at constant angular velocity, with an initially *stationary* dipolar magnetic field that threads the surface and extends to $r \to \infty$ (i.e., the outer boundary in our numerical simulations).

Specifically, the initial magnetic field is set via the vector potential

$$A_\phi = \frac{\mu \varpi^2}{r^3}; \quad A_r = A_\theta = 0, \tag{23}$$

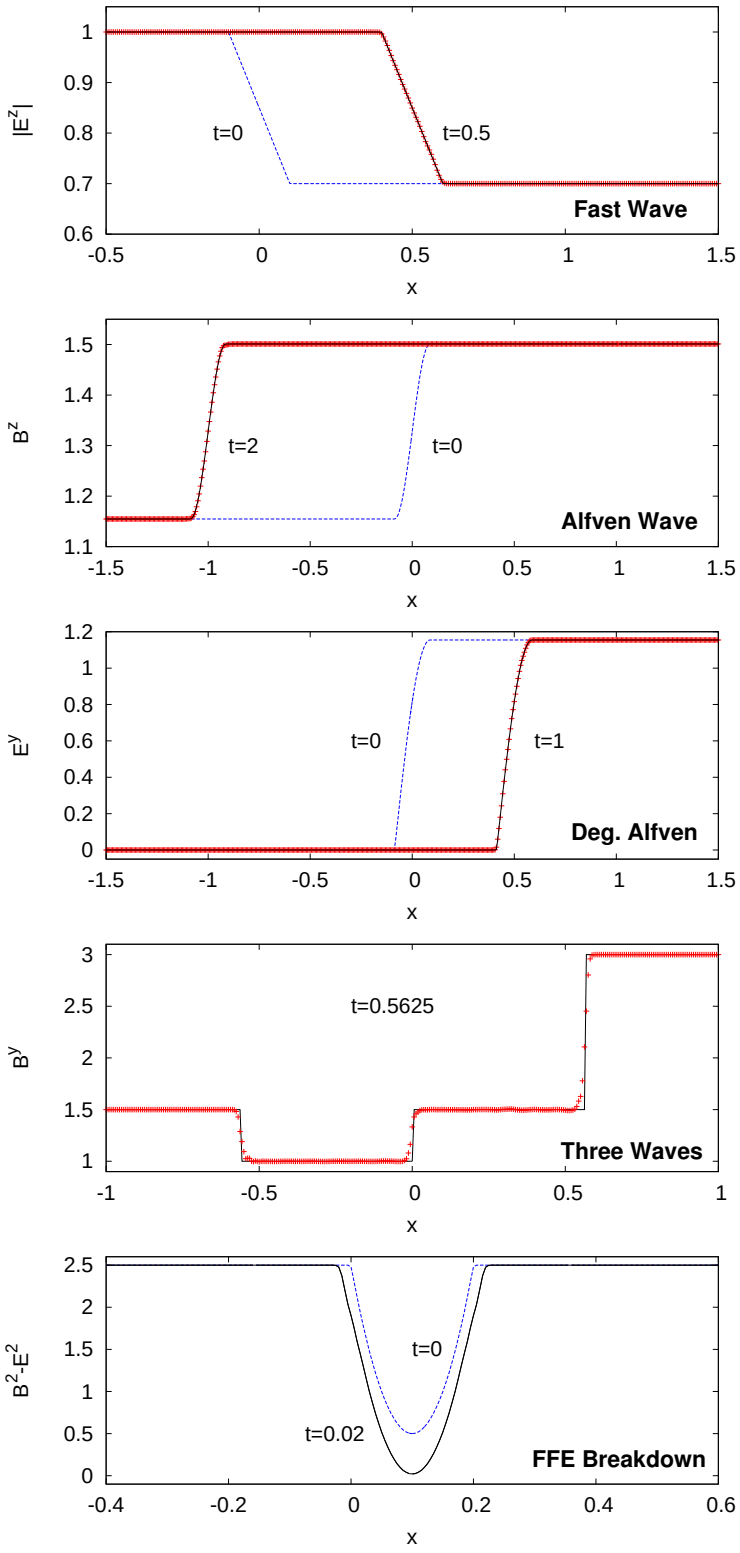

Figure 1: Summary of 1D test results. In the top four panels, initial data are shown as dashed blue lines. At later times, the analytic solution and the numerical solution are shown as solid black lines and red crosses respectively. The bottom panel shows the numerical solution as a solid black line. Figure formatting and numerical grid resolutions duplicate that of Ref. [43] so that direct comparisons can be made.

where $\mu = B_p R_{\rm NS}^3/2$, $R_{\rm NS}$ is the stellar radius, and $\varpi = \sqrt{x^2+y^2}$ the cylindrical radius. The velocity field at the surface and inside the "star" is set to be a solid-body rotator:

$$\mathbf{v} = \Omega \mathbf{e}_z \times \mathbf{r}, \tag{24}$$

where $\mathbf{e}_z$ is the unit vector in the z-direction, and Ω is the angular velocity of the star. We set $\Omega = 0.2$ such that the light cylinder is located at $R_{\rm LC} = 5R_{\rm NS}$, as in [43].

Since the solution in this test involves a current sheet within the light cylinder on the equatorial plane, i.e., on the $z = 0$ plane, we apply our strategy for handling current sheets as outlined in Step 4 of `GiRaFFE`'s core numerical algorithm (Sec. 3).

After starting the simulation, `GiRaFFE` quickly reproduces known features from the stationary solution of Contopoulos *et al* [15]. These features were later corroborated via the MHD simulation of Komissarov [28] and the FFE simulation of McKinney [31]. In short, the surface of the solid-body rotation of the stellar surface spins up the magnetic field lines in the magnetosphere to the same angular frequency as the stellar surface. In Fig. 2, we show that the angular frequency of the magnetic fields closely tracks the angular velocity of the star, even out to $r = 0.7R_{\rm LC}$ *regardless of the angle at which* Ω *is measured at this radius*. And as $r \to R_{\rm LC}$, the magnetic field lines transition from dipolar in structure (left panel of Fig. 2) to an open field line configuration (center panel of Fig. 2).

4.2. Curved spacetime background tests

We perform a set of three curved-spacetime background tests: the split monopole, the exact Wald solution, and the magnetospheric Wald solution. Initial data parameters are summarized in Table 3, and the grid setups are presented in Table 4. Testing procedures largely follow that outlined in Ref. [43], in which plasma dynamics are modeled near a BH in "shifted Kerr-Schild" coordinates (i.e., Kerr-Schild coordinates but with the radial coordinate shifted to minimize the strong curvature near $r = 0$; see Appendix for full 3+1 decomposition). The equatorial current sheet plays an important role in these tests, and to prevent numerical dissipation intrinsic to our algorithms from quickly destroying the current sheet, the strategy of Ref.[30] is employed as described in Sec. 3.

4.2.1. Split Monopole The split monopole solution is derived from the Blandford-Znajek force-free monopole solution [8, 32], by inverting the solution in the lower hemisphere. The solution we use in the test is accurate only to first order in a and follows Refs. [26, 30, 43] in dropping problematic terms involving $f(r)$ and $f'(r)$. The test is performed in shifted Kerr-Schild radial coordinates (see Appendix) with radial shift $r_0 = 1.0M$, and with spin $a_* = a/M = J/M^2 = 0.1$ where M is the BH mass. One important property of this solution is that although initially all magnetic field lines penetrate the black hole horizon, later they escape from the ergosphere of the black hole. Therefore, a stable equatorial current sheet is required to sustain this configuration, otherwise the magnetic field lines reconnect and are pushed away [26]. The results of this test without resistivity and therefore, without reconnection, due to the equatorial

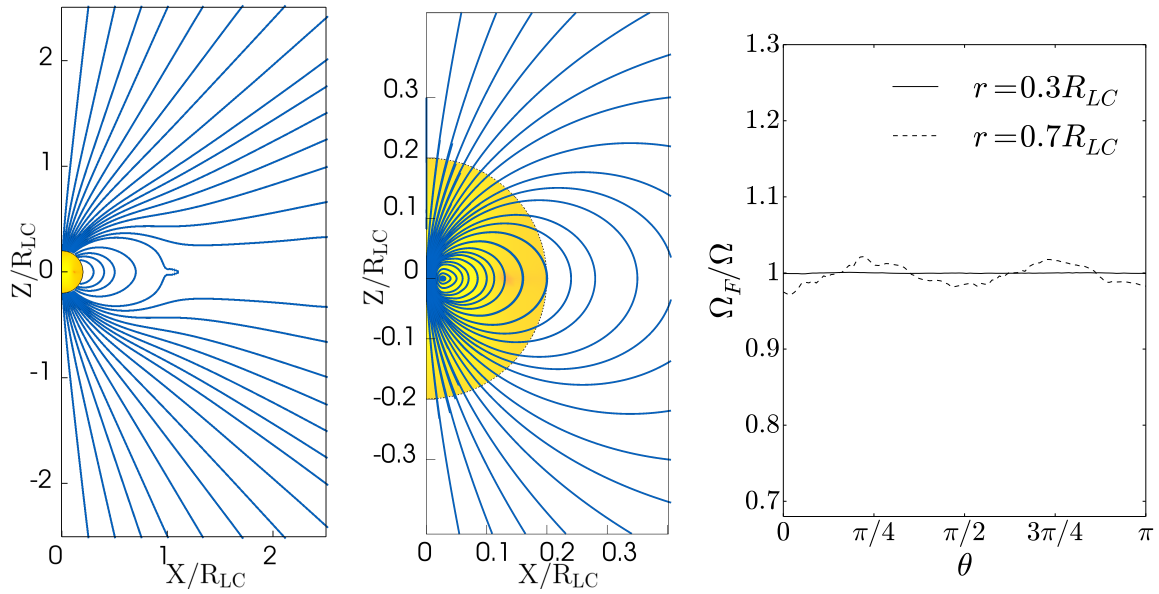

Figure 2: Aligned Rotator: a) Magnetic field structure after 3 rotation periods of the rotator. $R_{\rm LC}$ denotes light-cylinder radius. b) Magnetic field structure near the "star" (yellow circle; zoomed out in a)). c) Plasma orbital frequency at 30% and 70% the light-cylinder radius, versus the azimuthal angle θ. Figure formatting duplicates that of Ref. [43] so that direct comparison can be made, and we note that our grid structure corresponds most closely to their "low-resolution" case.

current sheet, are shown in Fig. 3, and are in good agreement with the ones obtained in Refs. [26, 30, 43].

4.2.2. Exact Wald This solution to Maxwell's equations, found by Wald [51], describes the electrovacuum around a rotating black hole immersed in a uniform magnetic field aligned with the axis of rotation of the black hole. Near the black hole, the solution contains both magnetic and electric fields, while far away the electric field vanishes. For a nonspinning ($a = 0$) black hole, this is also a force-free solution, which is the case considered in this test. Following Ref. [43], we choose Kerr-Schild coordinates with a radial shift $r_0 = 0.4M$ which yields a BH horizon located at $r = 1.6M$ (see Appendix for full 3+1 form of shifted Kerr-Schild spacetime).

Demonstrating convergence of the numerical to the exact solution in this case is complicated by the large region inside the horizon that violates the force-free condition $B^2 - E^2 > 0$. To wit, in Kerr-Schild coordinates Wald's solution yields

$$B^2 - E^2 = B_0^2 \left(1 - \frac{2M\sin^2(\theta)}{r}\right). \tag{25}$$

The horizon exists at $r = 2M$ in these (unshifted Kerr-Schild) coordinates, so in the equatorial plane ($\theta = \pi/2$), $B^2 - E^2 > 0$ is violated at all points $r \leq 2M$ - i.e., all

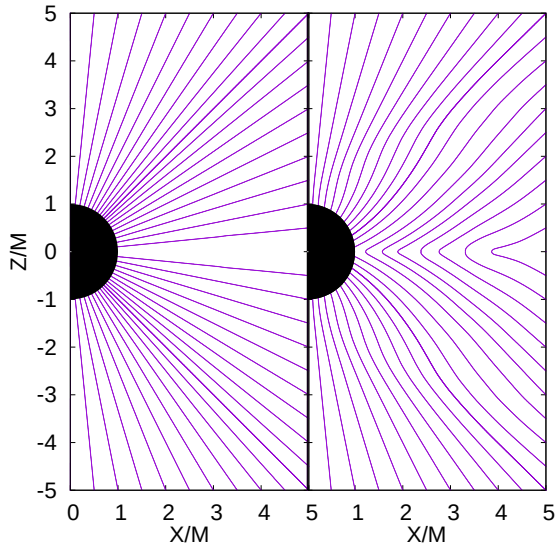

Figure 3: Split Monopole: Magnetic field structure at $t = 0M$ (left) and $t = 5M$ (right). Figure formatting duplicates that of Ref. [43] so that direct comparison can be made.

points inside the horizon, including the horizon itself. This has been noted previously by Komissarov [26].

As such, when we apply the GRFFE constraints (as described in Step 4 of Sec. 3) immediately after the initial data are set up at $t = 0$, all points where $B^2 - E^2 \leq 0$ *get overwritten to a solution inconsistent with the Wald solution.* Hence we have a *non-stationary* solution inside the horizon. But despite this abrupt replacement of data inside the horizon, Fig. 4 demonstrates the magnetic field lines at the initial time overlap the lines at $t = 5M$ extremely well, indicating excellent *qualitative* agreement of our numerical evolution with the stationarity of Wald's solution.

However, *quantitative* convergence of the numerical solution to the stationary (initial) solution near the horizon is strongly influenced by our code's correction of the $B^2 - E^2 > 0$ violation inside and at the horizon, which induces spurious, numerically-driven dynamics inside the horizon. Since numerical errors can propagate superluminally, these dynamics propagate outside the horizon and manifest as a numerical solution outside the horizon *inconsistent* with stationarity and result in a drop in the convergence order to the stationary solution within this region.

Therefore, to properly measure the order at which our numerical solution converges to the stationary solution, we must ignore the non-stationary region very close to the horizon. Our measurement strategy is as follows. For a given numerically-evolved quantity Q, we compute the L_2 norm of the difference between Q and its stationary value Q_0 (given by the Wald solution) as

$$\Delta Q = \sqrt{\int_{\mathcal{V}} \left(Q - Q_0\right)^2 d^3x}. \tag{26}$$

We choose a volume $\mathcal{V}$ that covers the entire numerical simulation domain, excising the

Res.	$\Delta A^x \cdot 10^4$	$\Delta A^y \cdot 10^4$	$\Delta A^z \cdot 10^5$	$\Delta(\psi^6\Phi) \cdot 10^4$
H	4.855	4.857	4.394	1.053
M	3.9·H	3.9·H	4.3·H	4.0·H
L	15.3·H	15.3·H	19.3·H	15.6·H

Res.	$\Delta v^x \cdot 10^4$	$\Delta v^y \cdot 10^4$	$\Delta v^z \cdot 10^5$	$\Delta B^x \cdot 10^4$	$\Delta B^y \cdot 10^4$	$\Delta B^z \cdot 10^4$
H	2.115	2.102	1.209	1.406	1.398	8.764
M	3.3·H	3.4·H	3.5·H	3.6·H	3.7·H	4.0·H
L	12.1·H	12.2·H	13.1·H	14.0·H	14.1·H	15.8·H

Table 5: L_2 norms of the difference between our numerical results and the initial data (Eq. 26) at $t = 5M$ for the 4-vector potential (top), and the velocity and magnetic field (bottom) at 3 resolutions. L, M, and H represent choice of numerical resolution, as defined in Table 4.

region $r < 8r_{\rm H}$, where $r_{\rm H}$ is the horizon radius in our shifted Kerr-Schild coordinates ($r_{\rm H} \approx 1.4M$). Additionally, to eliminate known low-order convergence contamination from the chosen approximate outer boundary conditions, the region $r > 90M$ is also excised.

Table 5 demonstrates that when adopting this measure, our numerical results converge to the stationary (initial) solution at approximately second order in numerical grid spacing (i.e., the error E is measured to scale as $E \sim {\Delta x_{\rm min}}^2$), which is expected from our choice of reconstruction scheme and AMR grid interpolation order.

4.2.3. Magnetospheric Wald The magnetospheric Wald problem, called the "ultimate Rosetta Stone" by Komissarov [26], yields insights about black hole magnetospheres beyond the Membrane Paradigm [49]. The Membrane Paradigm predicts that only a small fraction of magnetic field lines penetrating a spinning black hole's horizon will be dragged via Lens-Thirring into a co-rotating motion with the BH spin. The magnetospheric Wald problem is a clear counterexample to this prediction.

There is no known analytic solution to this problem as $t \to \infty$, but the initial data are expected to evolve into a steady, equatorially-symmetric state with a current sheet visible in the equatorial plane within the black hole ergosphere. The right panel of Fig. 4 shows the poloidal magnetic field lines at $t = 126M$, where the solution reaches a steady state, which agrees well with the state found in Refs. [26, 43]. As in Ref. [43], this test is performed in shifted Kerr-Schild radial coordinates with dimensionless spin $a_* = 0.9$ and radial shift $r_0 = 0.4359M$ selected so that the horizon radius is nearly one.

5. Conclusions and Future Work

We have presented code validation test results from our new code, `GiRaFFE`, which is the first open-source GRFFE code designed to model strongly-magnetized, tenuous plasmas in full general relativity. The GRFFE approximation is well motivated in many cases of astrophysical interest, including the launching of relativistic jets in BH and NS

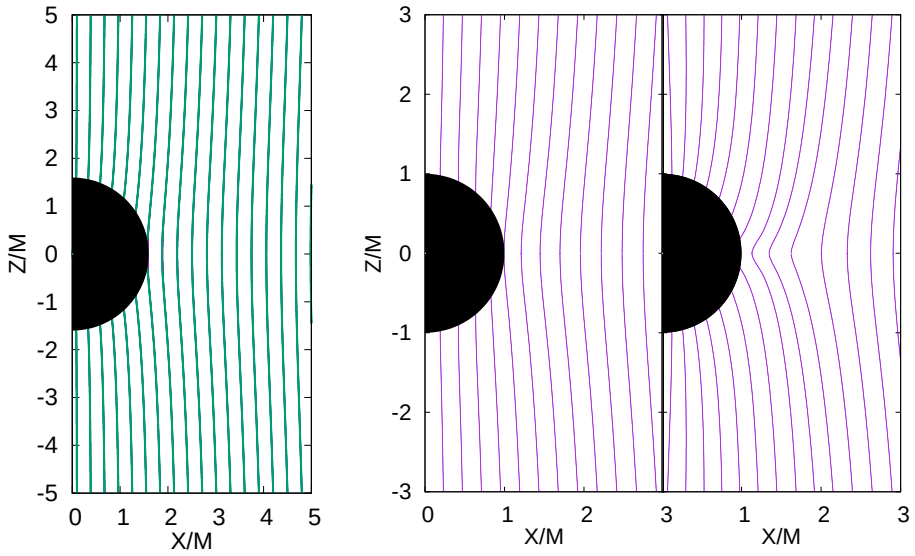

(a) (b)

Figure 4: a) Exact Wald: Magnetic field structure at $t = 5M$ (green) plotted atop exact solution (i.e., $t = 0$ data; purple). b) Magnetospheric Wald: Magnetic field structure at $t = 0M$ (left) and after reaching apparent equilibrium at $t = 126M$ (right). Figure formatting duplicates that of Ref. [43] so that direct comparisons can be made.

spacetimes, and the evolution of NS, pulsar, and BH magnetospheres both in isolation and when interacting with binary companions.

To validate this new code, it was subjected to a battery of tests in both flat and strongly-curved BH spacetimes. `GiRaFFE` successfully reproduces several classes of exact smooth and discontinuous wave solutions in one spatial dimension. We also demonstrated that for a test case in which a transition layer evolves from a state that satisfies the FFE conditions to one that violates them, `GiRaFFE` behaves in the expected manner. Moving from one to three spatial dimensions, we also verified that our code reproduces the known steady-state solution for the aligned rotator, which is frequently used to approximate pulsar magnetospheres.

A suite of three tests were performed in three spatial dimensions within a shifted-radius, Kerr-Schild curved spacetime background (as described in the Appendix), and endowed with a current sheet in the equatorial plane. All three cases evolved to known solutions, with the exact Wald test validating that our code is, as expected, second-order convergent to the exact solution. By passing this suite of tests, we have shown that `GiRaFFE` passes all of the validation tests adopted by the GRFFE codes of Refs. [30, 43]. `GiRaFFE` has therefore demonstrated its capacity for evolving force-free fields in dynamical spacetimes.

At present, `GiRaFFE` can perform purely force-free evolutions in the context of dynamical spacetime evolutions within the Einstein Toolkit/Carpet/McLachlan framework. In the future, we plan to integrate `GiRaFFE` with `IllinoisGRMHD`, so that

it can tackle problems that combine both GRMHD and GRFFE domains. This will involve the design and implementation of new GRMHD/GRFFE matching algorithms, and will likely benefit from the creation of a separate library containing common features of `GiRaFFE` and `IllinoisGRMHD`, to avoid unnecessary code duplication. As outlined throughout the text, there are a number of problems of astrophysical interest that `GiRaFFE` is ideally positioned to explore, and we hope the wider community will join us in these investigations by leveraging this new open-source tool.

Acknowledgements

We gratefully acknowledge I. Ruchlin and V. Paschalidis for valuable discussions as this work was prepared, as well as N. Gregg for technical assistance. This work was supported by NASA Grant 13-ATP13-0077 and NSF EPSCoR Grant 1458952. Large-scale computations were performed on West Virginia University's `Spruce Knob` supercomputer, funded in part by NSF EPSCoR Research Infrastructure Improvement Cooperative Agreement #1003907, the state of West Virginia (WVEPSCoR via the Higher Education Policy Commission), and West Virginia University. MBW wishes to acknowledge H.-I. Kim for technical assistance with part of the computations done in Korea for this work.

Appendix: 3+1 Black Hole Spacetime in Shifted Kerr-Schild Coordinates

A complete description of a black hole spacetime in Kerr-Schild spherical polar coordinates that includes an explicit analytic form of the extrinsic curvature for arbitrary spin parameters does not exist in the literature, so we first include it here for completeness. Then we present our strategy for transforming spacetime quantities into shifted Kerr-Schild Cartesian coordinates.

In unshifted spherical polar coordinates, where $\rho = r^2 + a^2\cos^2(\theta)$, M is the black hole mass, and a is the black hole spin parameter, the Kerr-Schild lapse, shift, and 3-metric are given by

$$\alpha = \frac{1}{\sqrt{1+\frac{2Mr}{\rho^2}}} \tag{A.1}$$

$$\beta^r = \alpha^2 \frac{2Mr}{\rho^2} \tag{A.2}$$

$$\beta^\theta = \beta^\phi = \gamma_{r\theta} = \gamma_{\theta\phi} = 0 \tag{A.3}$$

$$\gamma_{rr} = 1 + \frac{2Mr}{\rho^2} \tag{A.4}$$

$$\gamma_{r\phi} = -a\gamma_{rr}\sin^2(\theta) \tag{A.5}$$

$$\gamma_{\theta\theta} = \rho^2 \tag{A.6}$$

$$\gamma_{\phi\phi} = \left(r^2 + a^2 + \frac{2Mr}{\rho^2}a^2\sin^2(\theta)\right)\sin^2(\theta). \tag{A.7}$$

Next, we define a few useful quantities,

$$A = \left(a^2\cos(2\theta) + a^2 + 2r^2\right) \tag{A.8}$$

$$B = A + 4Mr \tag{A.9}$$

$$D = \sqrt{\frac{2Mr}{a^2\cos^2(\theta) + r^2} + 1}. \tag{A.10}$$

Then the extrinsic curvature $K_{ij} = (\nabla_i\beta_j + \nabla_j\beta_i)/(2\alpha)$ (see, *e.g.*, Eq. 13 in Ref. [16]) with $\partial_t\gamma_{ij} = 0$, may be written in spherical polar coordinates as

$$K_{rr} = \frac{D(A+2Mr)}{A^2B}\left[4M\left(a^2\cos(2\theta) + a^2 - 2r^2\right)\right] \tag{A.11}$$

$$K_{r\theta} = \frac{D}{AB}\left[8a^2Mr\sin(\theta)\cos(\theta)\right] \tag{A.12}$$

$$K_{r\phi} = \frac{D}{A^2}\left[-2aM\sin^2(\theta)\left(a^2\cos(2\theta) + a^2 - 2r^2\right)\right] \tag{A.13}$$

$$K_{\theta\theta} = \frac{D}{B}\left[4Mr^2\right] \tag{A.14}$$

$$K_{\theta\phi} = \frac{D}{AB}\left[-8a^3Mr\sin^3(\theta)\cos(\theta)\right] \tag{A.15}$$

$$K_{\phi\phi} = \frac{D}{A^2B}\Big[2Mr\sin^2(\theta)\left(a^4(r-M)\cos(4\theta) + a^4(M+3r) + \right. \tag{A.16}$$

$$\left. 4a^2r^2(2r-M) + 4a^2r\cos(2\theta)\left(a^2 + r(M+2r)\right) + 8r^5\right)\Big]. \tag{A.17}$$

All `GiRaFFE` curved-spacetime code validation tests adopt shifted Kerr-Schild Cartesian coordinates (x', y', z'), which map $(0, 0, 0)$ to the finite radius $r = r_0 > 0$ in standard (unshifted) Kerr-Schild spherical polar coordinates. So, in many ways, this is similar to a trumpet spacetime. Though this radial shift acts to shrink the black hole's coordinate size, it also renders the very strongly-curved spacetime fields at $r < r_0$ to vanish deep inside the horizon, which can contribute to numerical stability when evolving hydrodynamic, MHD, and FFE fields inside the horizon.

The shifted radial coordinate r' relates to the standard spherical polar radial coordinate r via $r = r' + r_0$, where $r_0 > 0$ is the (constant) radial shift.

As an example, to compute $K_{x'y'}$ at some arbitrary point (x', y', z'), we first convert the coordinate (x', y', z') into shifted spherical-polar coordinates via $(r' = \sqrt{x'^2 + y'^2 + z'^2}, \theta', \phi') = (r', \theta, \phi)$, as a purely radial shift like this preserves the original angles. Next, we evaluate the components of the Kerr-Schild extrinsic curvature K_{ij} (provided above) in standard spherical polar coordinates at $(r = r' + r_0, \theta, \phi)$. Defining $x^i_{\rm sph,sh}$ as the ith shifted spherical polar coordinate and $x^i_{\rm sph}$ as the ith (unshifted) spherical polar coordinate, $K_{x'y'}$ is computed via the standard coordinate transformations:

$$K_{x'y'} = \frac{dx^k_{\rm sph,sh}}{dx'}\frac{dx^l_{\rm sph,sh}}{dy'}\frac{dx^i_{\rm sph}}{dx^k_{\rm sph,sh}}\frac{dx^i_{\rm sph}}{dx^l_{\rm sph,sh}}K_{ij}. \tag{A.18}$$

However, we have $dx^i_{\rm sph} = dx^i_{\rm sph,sh}$, since the radial shift r_0 is a constant and the angles are unaffected by the radial shift. This implies that $dx^k_{\rm sph,sh}/dx' = dx^k_{\rm sph}/dx'$ and $dx^i_{\rm sph}/dx^k_{\rm sph,sh} = \delta^i_k$.

So after computing *any spacetime quantity* at a point $(r = r' + r_0, \theta, \phi)$, we need only apply the standard spherical-to-Cartesian coordinate transformation to evaluate that quantity in shifted Cartesian coordinates.

References

[1] B. P. Abbott, R. Abbott, T. D. Abbott, M. R. Abernathy, F. Acernese, K. Ackley, C. Adams, T. Adams, P. Addesso, R. X. Adhikari, and et al. GW151226: Observation of Gravitational Waves from a 22-Solar-Mass Binary Black Hole Coalescence. *Phys. Rev. Lett.*, 116(24):241103, June 2016.

[2] B. P. Abbott, R. Abbott, T. D. Abbott, M. R. Abernathy, F. Acernese, K. Ackley, C. Adams, T. Adams, P. Addesso, R. X. Adhikari, and et al. Observation of Gravitational Waves from a Binary Black Hole Merger. *Phys. Rev. Lett.*, 116(6):061102, February 2016.

[3] D. Alic, P. Moesta, L. Rezzolla, O. Zanotti, and J. L. Jaramillo. Accurate simulations of binary black-hole mergers in force-free electrodynamics. *Astrophys. J.*, 754:36, 2012.

[4] R. Arnowitt, S. Deser, and C. W. Misner. Dynamical Structure and Definition of Energy in General Relativity. *Phys. Rev.*, 116:1322–1330, December 1959.

[5] D. Balsara and D. S. Spicer. A staggered mesh algorithm using high order godunov fluxes to ensure solenoidal magnetic fields in magnetohydrodynamic simulations. *J. Comp. Phys.*, 149(2):270292, 1999.

[6] K. Belczynski, V. Kalogera, and T. Bulik. A Comprehensive Study of Binary Compact Objects as Gravitational Wave Sources: Evolutionary Channels, Rates, and Physical Properties. *Astrophys. J.*, 572:407–431, June 2002.

[7] E. Berger. Short-Duration Gamma-Ray Bursts. *Ann. Rev. Astron. Astrophys.*, 52:43–105, 2014.

[8] R. D. Blandford and R. L. Znajek. Electromagnetic extraction of energy from Kerr black holes. *Mon. Not. R. Astron. Soc.*, 179:433, 1977.

[9] J. D. Brown, P. Diener, O. Sarbach, E. Schnetter, and M. Tiglio. Turduckening black holes: an analytical and computational study. *Phys. Rev. D*, 79:044023, 2009.

[10] G. Cao, L. Zhang, and S. Sun. The spectral simulations of axisymmetric force-free pulsar magnetosphere. *Mon. Not. R. Astron. Soc.*, 455:4267, 2015.

[11] G. Cao, L. Zhang, and S. Sun. An oblique pulsar magnetosphere with a plasma conductivity. *Mon. Not. R. Astron. Soc.*, 461:1068, 2016.

[12] P. Colella and P. R. Woodward. The Piecewise Parabolic Method (PPM) for Gas-Dynamical Simulations. *J. Comp. Phys.*, 54:174–201, September 1984.

[13] Collaborative Effort. Einstein Toolkit for Relativistic Astrophysics. Astrophysics Source Code Library, February 2011.

[14] V. Connaughton, E. Burns, A. Goldstein, L. Blackburn, M. S. Briggs, B.-B. Zhang, J. Camp, N. Christensen, C. M. Hui, P. Jenke, T. Littenberg, J. E. McEnery, J. Racusin, P. Shawhan, L. Singer, J. Veitch, C. A. Wilson-Hodge, P. N. Bhat, E. Bissaldi, W. Cleveland, G. Fitzpatrick, M. M. Giles, M. H. Gibby, A. von Kienlin, R. M. Kippen, S. McBreen, B. Mailyan, C. A. Meegan, W. S. Paciesas, R. D. Preece, O. J. Roberts, L. Sparke, M. Stanbro, K. Toelge, and P. Veres. Fermi GBM Observations of LIGO Gravitational-wave Event GW150914. *Astrophys. J. Lett.*, 826:L6, July 2016.

[15] I. Contopoulos, D. Kazanas, and C. Fendt. The Axisymmetric Pulsar Magnetosphere. *Astrophys. J.*, 511 (1):351, 1999.

[16] G. B. Cook. Initial data for numerical relativity. *Living Rev. Relativity*, 3(1):5, 2000.

[17] L. Del Zanna, N. Bucciantini, and P. Londrillo. An efficient shock-capturing central-type scheme for multidimensional relativistic flows. II. Magnetohydrodynamics. *Astron. Astrophys.*, 400:397–413, March 2003.

[18] S. D. Drell, H. M. Foley, and M. A. Ruderman. Drag and Propulsion of Large Satellites in the Ionosphere: An Alfvén Propulsion Engine in Space. *J. Geophys Res*, 70:3131–3145, July 1965.

[19] Z. B. Etienne, V. Paschalidis, R. Haas, P. Mösta, and S. L. Shapiro. IllinoisGRMHD: an open-source, user-friendly GRMHD code for dynamical spacetimes. *Class. Quantum Grav.*, 32(17):175009, September 2015.

[20] Z. B. Etienne, V., Y. T. Liu, and S. L. Shapiro. Relativistic magnetohydrodynamics in dynamical spacetimes: Improved electromagnetic gauge condition for adaptive mesh refinement grids. *Phys. Rev. D*, 85:024013, 2012.

[21] B. D. Farris, R. Gold, V. Paschalidis, Z. B. Etienne, and S. L. Shapiro. Binary black hole mergers in magnetized disks: simulations in full general relativity. *Phys. Rev. Lett.*, 109:221102, 2012.

[22] P. Goldreich and D. Lynden-Bell. Io, a jovian unipolar inductor. *Astrophys. J.*, 156:59–78, April 1969.

[23] A. Harten, P. D. Lax, and B. J. van Leer. On Upstream Differencing and Godunov-Type Schemes for Hyperbolic Conservation Laws. *SIAM Rev.*, 25:35–61, 1983.

[24] S. Husa, I. Hinder, and C. Lechner. Kranc: a Mathematica package to generate numerical codes for tensorial evolution equations. *Comput. Phys. Commun.*, 174:983–1004, June 2006.

[25] S. S. Komissarov. Time-dependent, force-free, degenerate electrodynamics. *Mon. Not. R. Astron. Soc.*, 336(3):759, 2002.

[26] S. S. Komissarov. Electrodynamics of black hole magnetospheres. *Mon. Not. R. Astron. Soc.*, 350:407, 2004.

[27] S. S. Komissarov. Observations of the Blandford-Znajek and the MHD Penrose processes in computer simulations of black hole magnetospheres. *Mon. Not. R. Astron. Soc.*, 359:801, 2005.

[28] S. S. Komissarov. Simulations of the axisymmetric magnetospheres of neutron stars. *Mon. Not. R. Astron. Soc.*, 367:19, 2006.

[29] Kranc: Kranc assembles numerical code, http://kranccode.org/.

[30] J. C. McKinney. General relativistic force-free electrodynamics: A new code and applications to black hole magnetospheres. *Mon. Not. R. Astron. Soc.*, 367:1797, 2006.

[31] J. C. McKinney. Relativistic force-free electrodynamic simulations of neutron star magnetospheres. *Mon. Not. R. Astron. Soc.*, 368:L30, 2006.

[32] J. C. McKinney and C. F. Gammie. A measurement of the electromagnetic luminosity of a Kerr black hole. *Astrophys. J.*, 611:977, 2004.

[33] S. T. McWilliams and J. Levin. Electromagnetic Extraction of Energy from Black-hole-Neutron-star Binaries. *Astrophys. J.*, 742:90, December 2011.

[34] E. Nakar. Short-Hard Gamma-Ray Bursts. *Phys. Rept.*, 442:166–236, 2007.

[35] A. Nathanail and I. Contopoulos. Black hole magnetospheres. *Astrophys. J.*, 788(2):186, 2014.

[36] C. Palenzuela. Modelling magnetized neutron stars using resistive magnetohydrodynamics. *Mon. Not. R. Astron. Soc.*, 431:1853, 2013.

[37] C. Palenzuela, C. Bona, L. Lehner, and O. Reula. Robustness of the Blanford-Znajek Mechanism. *Class. Quantum Grav.*, 28:4007, 2011.

[38] C. Palenzuela, T. Garrett, L. Lehner, and S. L. Liebling. Magnetospheres of black hole systems in force-free plasma. *Phys. Rev. D*, 82:044045, 2010.

[39] K. Parfrey, A. M. Beloborodov, and L. Hui. Introducing PHAEDRA: a new spectral code for simulations of relativistic magnetospheres. *Mon. Not. R. Astron. Soc.*, 423(2):1416, 2012.

[40] V. Paschalidis. General relativistic simulations of compact binary mergers as engines of short gamma-ray bursts. *ArXiv e-prints*, 1611.01519, 2016.

[41] V. Paschalidis, Z. B. Etienne, and S. L. Shapiro. General-relativistic simulations of binary black hole-neutron stars: Precursor electromagnetic signals. *Phys. Rev. D*, 88(2):021504, July 2013.

[42] V. Paschalidis, M. Ruiz, and S. L. Shapiro. Relativistic Simulations of Black Hole-Neutron Star Coalescence: The Jet Emerges. *Astrophys. J. Lett.*, 806:L14, June 2015.

[43] V. Paschalidis and S. L. Shapiro. A new scheme for matching general relativistic ideal magnetohydrodynamics to its force-free limit. *Phys. Rev. D*, 88:104031, 2013.

[44] J. Petri. General-relativistic force-free pulsar magnetospheres. *Mon. Not. R. Astron. Soc.*, 455(4):3779, 2016.

[45] J. Petri. Strongly magnetized rotating dipole in general relativity. *Astron. Astrophys.*, 594:A112, 2016.

[46] M. Ruiz, R. N. Lang, V. Paschalidis, and S. L. Shapiro. Binary Neutron Star Mergers: A Jet Engine for Short Gamma-Ray Bursts. *Astrophys. J. Lett.*, 824:L6, June 2016.

[47] E. Schnetter, S. Hawley, and I. Hawke. Carpet: Adaptive Mesh Refinement for the Cactus Framework. Astrophysics Source Code Library, November 2016.

[48] A. Spitkovsky. Time-dependent force-free pulsar magnetospheres: axisymmetric and oblique rotators. *Astrophys. J.*, 648:L51, 2006.

[49] K. S. Thorne, R. H. Price, and D. A. MacDonald. *Black holes: The membrane paradigm.* Yale University Press, 1986.

[50] G. Tóth. The $\nabla \cdot B = 0$ Constraint in Shock-Capturing Magnetohydrodynamics Codes. *J. Comp. Phys.*, 161:605–652, July 2000.

[51] R. M. Wald. Black hole in a uniform magnetic field. *Phys. Rev. D*, 10:1680, Sep 1974.

[52] F. Zhang, S. T. McWilliams, and H. P. Pfeiffer. Stability of exact force-free electrodynamic solutions and scattering from spacetime curvature. *Phys. Rev. D*, 92:024049, 2015.